Improved Hole Extraction and Band Alignment via Interface Modification in Hole Transport MaterialFree Ag/Bi Double Perovskite Solar Cells

Original
Improved Hole Extraction and Band Alignment via Interface Modification in Hole Transport MaterialFree Ag/Bi Double Perovskite Solar Cells / Schmitz, F., Bhatia, R., Burkhart, J., Schweitzer, P., Allione, M., Gallego, J., Piotrowski, P., Cajzl, J., Paszke, P., Mohan Das, G., Pawlak, D.A., Bella, F., Schlettwein, D., Lamberti, F., Meloni, S., Gatti, T.. - In: SOLAR RRL. - ISSN 2367-198X. - (2024), pp. 1-15. [10.1002/solr.202300965]

Publisher:
Wiley

Published
DOI:10.1002/solr.202300965

Improved hole extraction and band alignment *via* interface modification in HTM-free Ag/Bi double perovskite solar cells

Fabian Schmitz, Ribhu Bhatia, Julian Burkhart, Pascal Schweitzer, Marco Allione, Jaime Gallego, Piotr Piotrowski, Jakub Cajzl, Piotr Paszke, Gour Mohan Das, Dorota A. Pawlak, Federico Bella, Derck Schlettwein, Francesco Lamberti, Simone Meloni,* Teresa Gatti**

Fabian Schmitz, Julian Burkhart, Pascal Schweitzer, Jaime Gallego, Derck Schlettwein, Teresa Gatti
Center for Materials Research, Justus Liebig University, Heinrich-Buff-Ring 17, 35392 Giessen, Germany
E-mail: teresa.gatti@phys.chemie.uni-giessen.de

Ribhu Bhatia, Simone Meloni
Department of Chemical and Pharmaceutical Sciences, Università of Ferrara, Via Luigi Borsari 46, I-44121 Ferrara, Italy
E-mail: simone.meloni@unife.it

Pascal Schweitzer, Derck Schlettwein
Institute of Applied Physics, Justus Liebig University, Heinrich-Buff-Ring 16, 35392 Giessen, Germany

Marco Allione, Federico Bella, Teresa Gatti
Department of Applied Science and Technology, Politecnico di Torino, C.so Duca degli Abruzzi 24, 10129 Torino, Italy

Piotr Piotrowski, Jakub Cajzl, Piotr Paszke, Gour Mohan Das, Dorota A. Pawlak
Centre of Excellence ENSEMBLE3 sp. z o. o., Wólczyńska 133, 01-919 Warsaw, Poland

Francesco Lamberti
Department of Chemical Sciences, University of Padova, Via Marzolo 1, 35131 Padova, Italy
E-mail: francesco.lamberti@unipd.it

Francesco Lamberti
Department of Information Engineering, University of Padova, Via Gradenigo 6a, 35131 Padova, Italy

Keywords: Silver-bismuth double perovskites, HTM-free perovskite solar cells, lead-free perovskite solar cells, carbon-based perovskite solar cells, interfacial engineering

Abstract

Within one decade, lead-halide perovskite solar cells (LHPs) have reached power conversion efficiencies compatible with that of silicon solar cells. While in the beginning, they suffered from short device lifetimes, those have also been strongly improved over time. However, their content of toxic lead still poses a risk of environmental pollution and human health on exposure. The double perovskite $Cs_2AgBiBr_6$ offers the potential to be a lead-free alternative light-harvesting material. In this work, the fabrication of hole transport material (HTM)-free $Cs_2AgBiBr_6$-based solar cells is presented, in which the double perovskite surface is modified *via* a *n*-butylammonium post-treatment to create a 2D/3D mixed interface. Additionally, the

commonly utilized metal electrode and HTM are substituted with a carbon black back electrode (CBE) consisting of up-cycled biowaste. Through the 2D/3D interface modification, charge recombination is suppressed, and band alignment is improved at the perovskite/CBE interface. Additionally, DFT calculations reveal that an increasing 2D modification thickness enhances the probability for holes in $Cs_2AgBiBr_6$ to be located close to the perovskite/CBE interface, further supporting their extraction. Overall, the power conversion efficiency of the HTM-free solar cells is improved, through the implementation of a low-cost, end-of-waste fabrication strategy.

1. Introduction

As the global energy demand is continuously increasing, renewable energies have gained large importance, since fossil fuels are limited, are a health hazard due to air pollution, and are the major source of global greenhouse-gas emission, resulting in anthropogenic global warming.[1,2] Since solar energy is the most abundant energy source on earth,[3] photovoltaics (PV) have the potential to play a crucial role in saturating the world's increasing energy demand.

Amongst several available absorbers for PV, hybrid organic-inorganic lead halide perovskites (LHPs) have attracted significant attention in recent years due to their combined features of large absorption coefficients,[4,5] high charge carrier lifetimes[6–10] and mobilities,[10,11] high defect tolerance,[11,12] as well as a convenient bandgap tunability.[4,13,14] Those properties enabled the fabrication of highly efficient photovoltaics (PVs) not only for outdoor,[5–8,10,13] but also for indoor applications,[15–17] under which they achieved power conversion efficiencies (PCEs) of up to 26.1%[18] and 41.2%,[19] respectively. However, lead harbors a health hazard,[20,21] which especially limits the application possibilities of LHPs.

When the divalent lead is substituted from the ABX_3 perovskite structure by stoichiometric amounts[22] of monovalent silver and trivalent bismuth, the elpasolite (broadly named double perovskite [DP]) $Cs_2AgBiBr_6$ is formed, a material that possesses high environmental stability[23–25] and drastically reduced toxicity, in comparison to LHPs.[26] Like LHPs, this DP features long charge carrier lifetimes[27–29] and can easily be solution-processed.[30–32] Yet, the PCEs of solar cells that are based on pristine $Cs_2AgBiBr_6$ as sole light-harvesting material have not exceeded 2.81%[33] due to a large indirect bandgap,[23,32,34] strong electron-phonon coupling,[31,35,36] short electron diffusion length[37,38] and an unfavorable polaron-hopping transport mechanism.[28,39,40] Also, the role of the $Cs_2AgBiBr_6$ crystallization to form thin films for well-performing solar cells is still not understood: thin films of pristine $Cs_2AgBiBr_6$ with comparable thicknesses and homogeneities result in reported solar cells with PCEs ranging from below 1% to above 2% despite equal solar cell architectures.[38,41–49] Sirtl et al. revealed in their work that low selectivity of the HTM supports recombination and therefore hampers the solar cell performance, due to insufficient band alignment, i.e. the absence of an electron barrier between perovskite and HTM.[50] Thus, they exposed a critical bottleneck of $Cs_2AgBiBr_6$-based solar cells. One common strategy to tackle the low selectivity and improve the band alignment between perovskite layers and HTM (and electron transport layers [ETLs] in inverted solar cells) is creating a two-dimensional (2D) perovskite interlayer.[46,51,52] When the dimensionality of a perovskite crystal is reduced from three-dimensional (3D) to 2D, it undergoes quantum confinement that increases its bandgap with decreasing layer thickness.[53–55] In detail, the valence band maximum (VBM) is slightly elevated and the conduction band minimum (CBM) is strongly elevated. When the 2D layer is utilized as an interlayer between the perovskite layer and the HTM, the high CBM level serves as an energy barrier that suppresses the injection of excited electrons from the perovskite layer into the HTM.[52,56] However, the VBM and CBM elevation of a 2D interlayer can not only improve the band alignment between perovskite and HTM but also allow the removal of the HTM to fabricate HTM-free perovskite solar cells. In the latter case, the 2D interlayer adopts the HTM's purpose of blocking electron extraction into the back electrode and improving the valence band (VB) alignment towards the back electrode. The schematic band diagrams of a $Cs_2AgBiBr_6$ solar cell with HTM as well as of HTM-free solar cells with and without a 2D perovskite layer are depicted in **Figure 1**. While the removal of the HTM causes increased recombination at the back electrode in a pure $Cs_2AgBiBr_6$ solar cell (Figure 1b), the presence of a 2D layer (Figure 1c) will improve the selectivity and the band alignment towards the back electrode. Thereby, the 2D modification adopts the function of the HTM.

Dimensional reduction from 3D to 2D has already been reported for $Cs_2AgBiBr_6$ by introducing large organic cations to substitute Cs.[57–60] Furthermore, Sirtl *et al.* carried out a post-treatment of $Cs_2AgBiBr_6$ thin films with phenethylammonium (PEA) bromide solution in which PEA substituted Cs in the top layers, thus forming a 2D capping layer.[46] Accordingly, the 2D modified surface of the perovskite films enhanced the valence band alignment and the selectivity towards the HTM 2,2′,7,7′-tetrakis-(*N*,*N*-di-4-methoxyphenylamino)-9,9′-spirobifluorene (Spiro-OMeTAD) which resulted in improved solar cells. The transformation of the upper layers of 3D perovskite thin films into 2D capping layers *via* ion exchange within a 2-step spin-coating process represents a commonly applied strategy for hybrid organic-inorganic LHPs.[51,61–64] We present the modification of $Cs_2AgBiBr_6$ with n-butylammonium (BA) to form a 2D capping layer and its application in HTM-free perovskite solar cells. BA was chosen to substitute Cs since in previous work, thin films of the 2D monolayered perovskite $(BA)_4AgBiBr_8$ (full substitution of Cs with BA) were characterized by enhanced homogeneity as well as a strongly differing work function in comparison to $(PEA)_4AgBiBr_8$.[58]

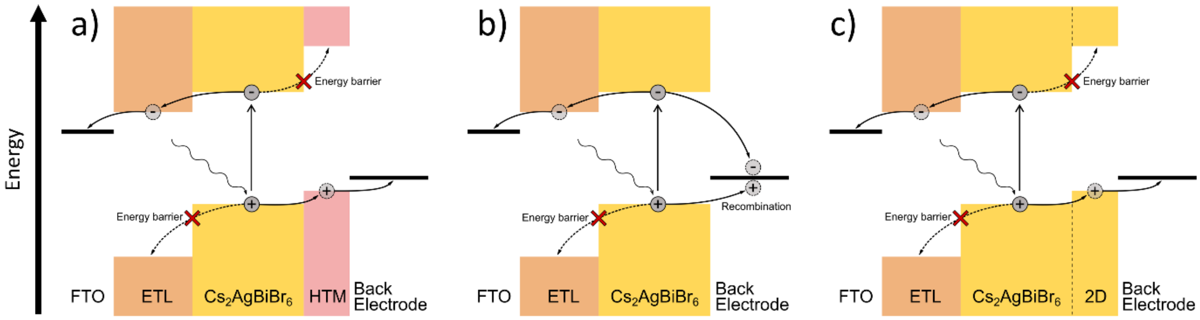

Figure 1. Schematic band diagrams of $Cs_2AgBiBr_6$ solar cell architectures. a) Classical n-i-p architecture in which $Cs_2AgBiBr_6$ is sandwiched between ETL and HTM, e.g., TiO_2 and Spiro-OMeTAD, respectively. The HTM creates an energy barrier for electrons and the band alignment favors the hole drift towards the back electrode. b) HTM-free $Cs_2AgBiBr_6$ solar cell. No energy barrier prevents the recombination of electrons and holes at the back electrode. c) 2D/3D surface modified $Cs_2AgBiBr_6$ solar cell. The 2D perovskite functions like an HTM, elevating the VBM slightly and the CBM strongly as will be shown in this work.

In this work, we thoroughly investigate the extent of conversion from $Cs_2AgBiBr_6$ towards a mixed 2D/3D phase when treating $Cs_2AgBiBr_6$ with different concentrations of BABr precursor solutions. Through a combination of structural, optical, and electrochemical analysis, we reveal the processes leading to enhanced PCEs in 2D/3D modified $Cs_2AgBiBr_6$ PVs and identify the best conditions for carrying out such modification. Simulations were performed to validate some hypotheses on the effect of $(BA)_4AgBiBr_8$. In particular, we focused on the effect of the concentration of BABr precursor solutions. Additionally, we combined the 2D surface modification with the application of a carbon-based electrode (CBE) to substitute both the HTM and the metal electrode. Through the introduction of a 2D interlayer between $Cs_2AgBiBr_6$ and CBE, we introduce both an additional energy barrier for electrons to suppress recombination at the perovskite/CBE interface and an improved band alignment to enhance the hole injection into the CBE. We remark once more that the objective of this work is not to obtain the most efficient $Cs_2AgBiBr_6$-based PV devices, which are typically obtained with a gold electrode, a Spiro-OMeTAD HTM, etc. Rather, we aim at making a step forward in the direction of cheap devices, by replacing altogether two expensive components of DP PV with alternative components, CBE and 2D modification of the 3D $Cs_2AgBiBr_6$ film. Moreover, not only will the utilization of CBEs and the removal of the HTM drastically reduce the material and fabrication costs of solar cells[65,66] but the carbon black in our CBE was even obtained from hazelnut shells, an industrial waste product. Thus, the presented solar cells serve as an end-of-waste design for low-toxic, low-cost perovskite solar cells.

2. Results and Discussion

$Cs_2AgBiBr_6$ thin films were fabricated by spin-coating in an argon-filled glovebox as described in the Experimental Section. The perovskite layers were deposited onto mesoporous TiO_2 (see **Figure S1**) since it was reported to enable enhanced charge collection compared to compact TiO_2.[38,50] To create 2D/3D mixed perovskites, the $Cs_2AgBiBr_6$ thin films were covered with BABr, dissolved in isopropanol at various concentrations (0.01 м, 0.05 м, and 0.1 м), spin-coated, and then left to dry overnight inside the glovebox. A sketch of the preparation process is depicted in **Figure 2**. For the sake of readability, samples treated with 0.01 м, 0.05 м, and 0.1 м BABr solution will be abbreviated as 0.01M, 0.05M, and 0.1M, respectively, throughout the report. We remark that our focus is the effect of the 2D post-treatment, particularly, the 2D/3D mixed perovskite in conjunction with a CBE which is obtained from byproducts of other (agricultural/food) industries. The devices fabricated and used in this work, including the reference devices based on the HTM Spiro-OMeTAD and a gold back electrode, are not optimized to achieve top efficiencies, e.g., adding passivating agents regularly used in the literature, or adopting careful deposition methods (see, for example, reference[67] and references cited therein). This is in line with the objective of exploring approaches to develop PV for markets requiring very low-cost devices.[68]

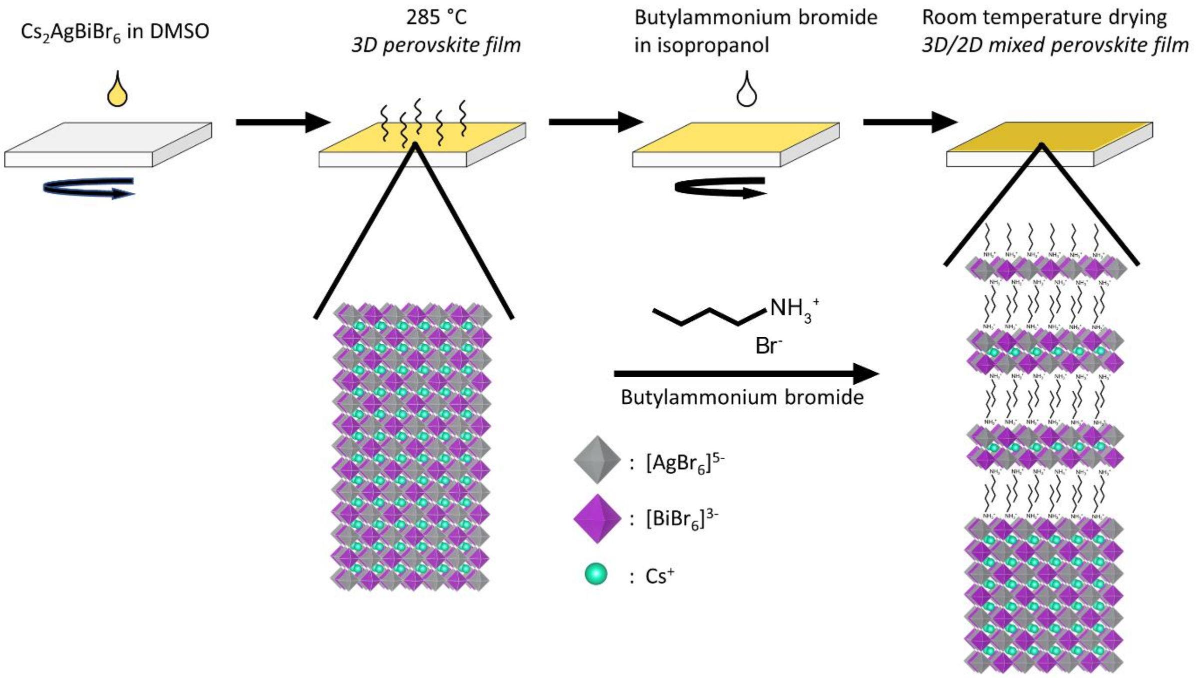

Figure 2. Schematic representation of the process used to produce 2D/3D interfaces in $Cs_2AgBiBr_6$ thin films.

We performed grazing-incidence x-ray diffraction (GIXRD) measurements on the thin films, as shown in **Figure 3**a, to detect the formation of a 2D phase within the $Cs_2AgBiBr_6$ thin film. For all thin films, the reflections of the 3D perovskite $Cs_2AgBiBr_6$ can be observed. Their shapes and positions are not affected by the BABr treatment, and no side phases are created due to this process. This also underlines that after the BABr treatment, bulk $Cs_2AgBiBr_6$ is still the dominant material in the thin films. While no differences between the pure 3D DP thin film and the 0.01M one can be detected, a weak reflection at around 4.5° appears for the 0.05M thin film, which can be correlated to the bilayer 2D phase $(BA)_2CsAgBiBr_7$.[57] For the 0.1M film, the intensity of this reflection strongly increases. Additionally, a second reflection at 6.1° appears which can be attributed to BABr residues that are still present on the thin film's surface. Interestingly, no reflections of the monolayer phase can be observed in either sample, which would appear at 6.5°.[57,58] It is important to note that the missing reflection for 0.01M does not rule out the formation of non-periodic 2D phases with lower or higher inorganic slab thicknesses due to the character of x-ray diffraction (XRD) in which reflections can only occur when periodicity is present.

The transmission UV-visible (UV-Vis) absorption spectra of all samples, depicted in Figure 3b, possess the typical shape of $Cs_2AgBiBr_6$ that is characterized by a resonant absorption feature at 448 nm and whose origins are still debated in the literature.[31,69] The overall absorbance decreases with increasing concentration of the BABr solution. We attribute this behavior to the enhanced conversion of 3D $Cs_2AgBiBr_6$ into 2D phases as observed by GIXRD which leaves less $Cs_2AgBiBr_6$ to absorb. To verify that the $Cs_2AgBiBr_6$ was lost due to conversion into 2D phases and not to its dissolution in isopropanol from the BABr solution treatment, we performed the same treatment with pure isopropanol (without BABr addition). Since the spectra before and after this control treatment do not differ and the perovskite layer thicknesses are independent of the 2D modification (see **Figure S2**), we assume the absorbance loss to solely stem from enhanced 3D/2D conversion.

2D perovskites feature an increased hydrophobicity due to the incorporation of organic ions.[70–72] As a consequence, 2D surface-modified 3D perovskites have been reported to better withstand humid conditions, due to their enhanced surface hydrophobicity.[73,74] Even though DP films typically show no such problems of chemical instability, changes in wettability by subsequent coatings will have consequences for contact formation. To investigate this effect on the $Cs_2AgBiBr_6$ thin films after BABr treatment, we performed contact angle measurements which are shown in **Figure S3** in the Supporting Information. The contact angle of the pure $Cs_2AgBiBr_6$ thin film with water is 18°, whereas the contact angle for all 2D modified thin films is increased to 51-52° due to the hydrophobicity of the BA. Although we observed the formation of increased amounts of the bilayer phase with increasing BABr concentration from GIXRD, the contact angle is independent of the amount of 2D phase that was formed. Therefore, we assume that the perovskite layer's surface is either already transformed into 2D phase for 0.01M or the surface of $Cs_2AgBiBr_6$ is covered with BA^+ ions which enhance the thin film hydrophobicity. An increased BABr concentration then leads to further phase transition of bulk $Cs_2AgBiBr_6$ at the surface and progressing into the film (see Figure 2).

In Figure 3c, a cross-section scanning electron microscopy (SEM) image of a $Cs_2AgBiBr_6$ solar cell with a CBE is depicted. The perovskite layer has a thickness of around 200 nm (yellow) and the CBE has a thickness of around 4 µm (red). Cross-section SEM images of the 2D/3D-modified $Cs_2AgBiBr_6$ layers are shown in Figure S2 in the Supporting Information. Independent of the 2D/3D modification, the perovskite layers possess thicknesses of around 200 nm. Top-view SEM images of the pure $Cs_2AgBiBr_6$ thin film and the different modifications, shown in Figure 3d and S4, give information about the surface morphology as well as about the extent of BABr residues that remain on the thin films after the treatment, respectively. For the pure $Cs_2AgBiBr_6$, an almost pinhole-free homogeneous film can be observed, that consists of 100-300 nm large grains. When the 0.01 M BABr treatment is conducted, few BABr residues (dark regions in **Figure S4**) can be found on the film surface and the perovskite grains are now characterized by a terrace-like morphology, that was already observed for thin films of pure 2D layered DPs.[58] This terrace-like character is even more pronounced for 0.05M and 0.1M, which follows the enhanced transformation from $Cs_2AgBiBr_6$ into a 2D phase with increased BABr concentration. Because of both the increased contact angle of 0.01M and the presence of the terrace-like structure, we assume that the phase transformation already takes place on the perovskite surface, despite missing evidence in GIXRD. Furthermore, for 0.05M, small grains start to grow on top of the perovskite grains. The amount and size of those small grains drastically increase for the 0.1M sample. We exclude recrystallization of $Cs_2AgBiBr_6$ due to the isopropanol post-treatment as the origin of the smaller grains, since they cannot be observed for 0.01M. However, due to the intense reflection that we observed from GIXRD analysis, we link those grains to the further growth of the 2D $(BA)_2CsAgBiBr_7$. It is important to note that the coverage of the perovskite films by BABr residues (Figure S4) drastically increases with the BABr concentration during the post-treatment of the $Cs_2AgBiBr_6$ thin films. We expect the contamination to be BABr residues due to the presence of a BABr reflection in GIXRD for 0.1M. These residues could not be removed by an additional washing step with isopropanol after BABr treatment.

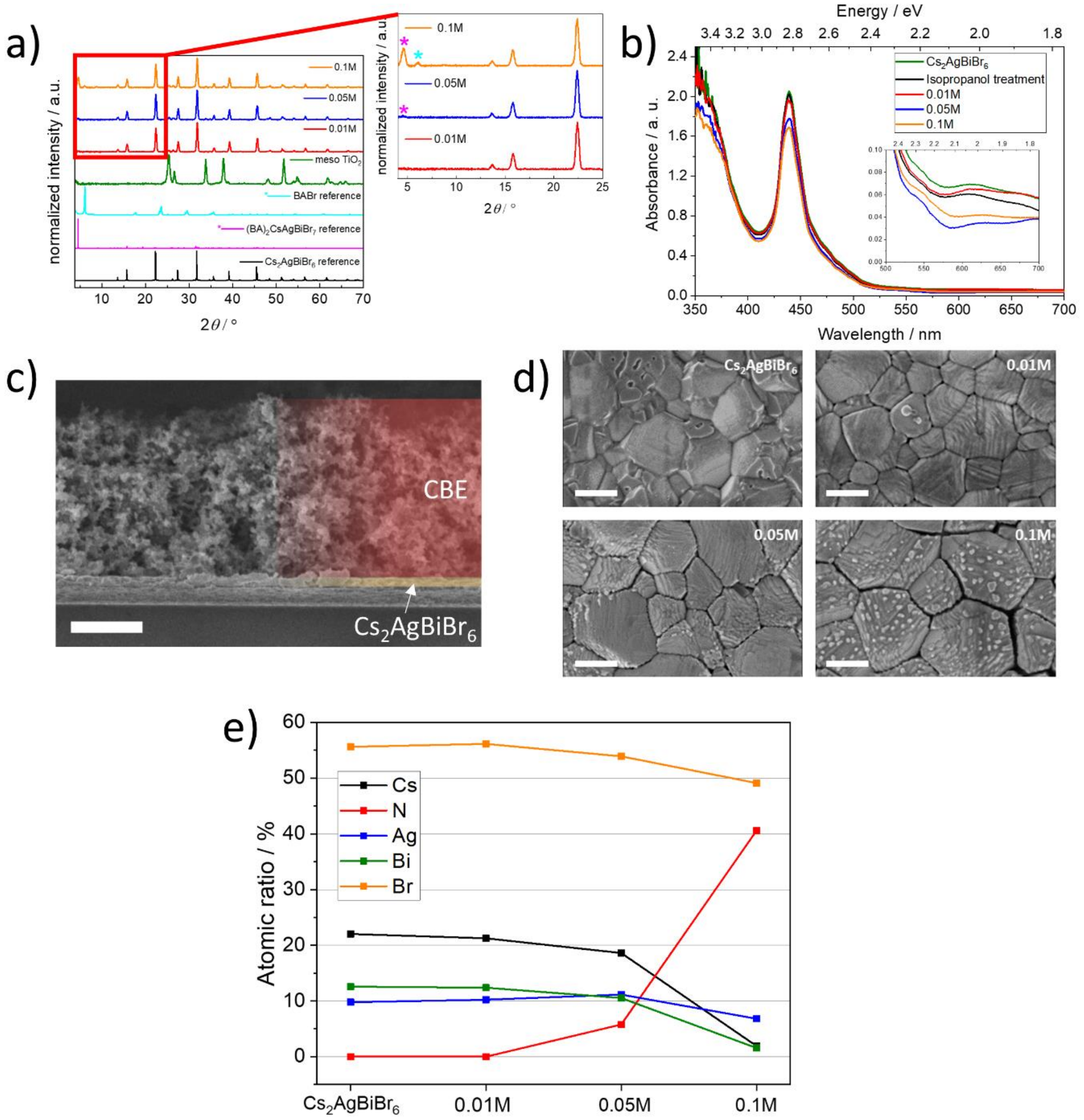

Figure 3. Physico-chemical characterization of the 2D/3D modified $Cs_2AgBiBr_6$ thin films at different BABr concentrations. a) GIXRD diffractograms of the 2D/3D modified thin films, with zoom on low angles region. b) UV-Vis absorption spectra of the 2D/3D modified thin films, of the reference and a reference film treated with only isopropanol. c) Cross-section SEM of a $Cs_2AgBiBr_6$ solar cell (scale is 2 µm). d) top-view SEM images of the 2D/3D modified thin films and the reference DP film. Top-view SEM scales are 200 nm, each. e) Surface elemental composition as measured through XPS on the reference and modified films.

We analyzed the surface compositions of the BABr-treated samples using x-ray photoelectron spectroscopy (XPS), as shown in Figure 3e. The elemental composition of the un-modified $Cs_2AgBiBr_6$ matches its sum formula. No difference in composition can be observed for 0.01M. However, an analysis of the elemental core levels of Cs, Ag, Bi, and Br, shown in **Figure S5**, reveals a binding energy shift of −0.1 eV from $Cs_2AgBiBr_6$ towards 0.01M. Such shifts stem from the increased electron densities of those elements due to the presence of the organic spacer cations and, therefore, are additional proof of the 2D phase formation and their tight binding with the 3D phases in 0.01M thin films.[75] Furthermore, for 0.05M, small amounts of nitrogen can be detected (see also **Figure S6**) while the composition of the other elements still equals the stoichiometry of $Cs_2AgBiBr_6$ within the significance of this method. The formation of large quantities of 2D phase, i.e. $(BA)_2CsAgBiBr_7$, would cause a decrease in Cs concentration. Thus, most of the XPS-detectable material is $Cs_2AgBiBr_6$, as the relatively weak $(BA)_2CsAgBiBr_7$ reflection in GIXRD suggests. Still, we report an enhanced binding energy shift in the core level spectra of −0.2 eV for Ag, Bi, and Br, and of −0.35 eV for Cs that underlines the enhanced phase transformation from $Cs_2AgBiBr_6$ into 2D phases. Furthermore, upward-shifted core level energies, equaling increased electron densities, amount to passivated ions. For 0.1M, the concentrations of Cs, Ag, and Bi strongly decrease while the concentration of Br only decreases slightly, and the concentration of N drastically increases to almost equal that of Br. This matches the observations from GIXRD and SEM that the surface of the thin film is covered by BABr residues. Furthermore, the high Cs, Ag, Bi, and Br concentrations, and the relatively low N concentration for the 0.05M film, detected *via* surface-sensitive XPS analysis, reveal that the amount of BABr residues is far lower than the SEM images make it appear.

To further prove the presence of BA in the material, we performed infrared (IR) spectroscopy on $Cs_2AgBiBr_6$ and 2D/3D modified thin films, as well as on a reference substrate that was not covered with a perovskite thin film, depicted as Fourier-transformed IR (FTIR) spectra in **Figure S7**. While the spectra of $Cs_2AgBiBr_6$ and the reference substrate show no differences, for 0.05M and 0.1M the absorbance at high wavenumbers gradually increases with a maximum at 2950 cm^{-1} which can be attributed to C-H stretching vibration due to the increasing amount of BA in the samples. For 0.01M, only a weak signal at 2950 cm^{-1} can be observed due to the much lower BA content compared to 0.05M and 0.1M.

We compared high-resolution transmission electron microscopy (HRTEM) cross-sections of a $Cs_2AgBiBr_6$ and a 0.05M thin film (**Figure S8**a and S8c), respectively. Like in the SEM cross-sections (Figure S2), the 2D modification is not distinctly observable for 0.05M. However, to investigate the loss of 3D phase at the thin film surface, we conducted energy dispersive x-ray spectroscopy (EDX) across both thin films, as shown in Figures S8b and S8d. As expected, the $Cs_2AgBiBr_6$ thin film showed a constant elemental distribution along the entire cross-section. On the other hand, for 0.05M, we observed a decay of Cs concentration towards the thin film surface while the Bi concentration stayed constant. We associate this behavior with the formation of Cs-poor 2D perovskite phases comparable to the XPS elemental analysis (see Figure 3e).

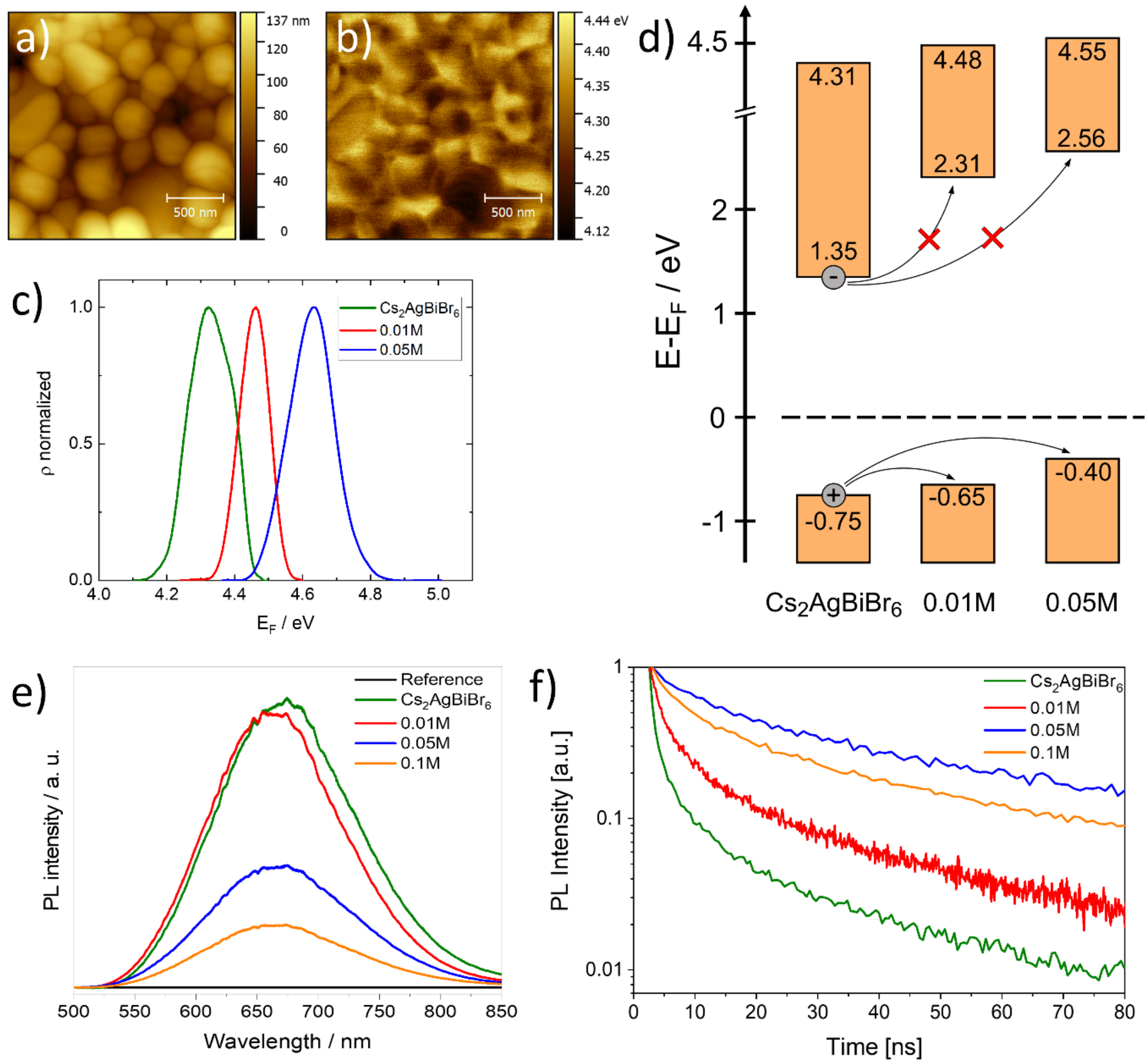

Figure 4. a) AFM and b) KPFM images of $Cs_2AgBiBr_6$. c) Work function distribution, calculated from KPFM images. d) Sketched band alignment between $Cs_2AgBiBr_6$, and 0.01M, or 0.05M, respectively. e),f) PL characterization of 2D/3D modified $Cs_2AgBiBr_6$ thin films and the reference one. e) SSPL and f) TRPL spectra recorded at room temperature (λ_{exc} = 405 nm).

Furthermore, we investigated the 2D modifications' impact on the perovskite's electronic structure, i.e., its VBM, CBM, and Fermi energy E_F, *via* XPS and KPFM. We prepared the respective perovskite layers on fluorine doped tin oxide (FTO)-covered glass substrates for this. The atomic force microscopy (AFM) as well as the related Kelvin probe force microscopy (KPFM) images of $Cs_2AgBiBr_6$ are shown in **Figure 4a** and 4b, respectively. KPFM and AFM of 0.01M, and 0.05M, are shown in **Figure S9** in the Supporting Information. The high amount of insulating BABr residues on the 0.1M surface prevents an AFM analysis and, therefore, a detailed and reliable analysis of the perovskite layer's Fermi energy. The AFM images match the observed homogeneity and grain sizes from the SEM images. Figure 4c shows that the average E_F, obtained from KPFM analysis, increases from $Cs_2AgBiBr_6$ (4.31 eV) to 0.01M (4.48 eV), and finally 0.05M (4.65 eV) with increasing 2D modification penetration depth.

To gather further information on how the 2D modification affects the perovskite/CBE band alignment, we performed XPS measurements. The energetic shift of the elemental core levels has already been discussed in a previous section. The valence shell energies as well as the extracted VB offsets towards E_F are depicted in **Figure S10** in the Supporting Information. It can be observed that the energetic difference between VBM and E_F is slightly reduced from pure $Cs_2AgBiBr_6$ (0.75 eV) towards 0.01M (0.65 eV) and strongly reduced for 0.05M (0.40 eV). The absolute VBM-E_F discrepancies as well as their enhancement for $Cs_2AgBiBr_6$ and 0.01M are similar to the values found by Sirtl *et al.* for their PEA 2D modification.[46] In contrast, we report a strongly improved band alignment for 0.05M. Using the E_F values from our KPFM analysis as well as an average literature bandgap of 2 eV for $Cs_2AgBiBr_6$ and a bandgap of 2.96 eV for the 2D bilayer[57] that is the dominant phase according to our GIXRD analysis, we created a band diagram of our $Cs_2AgBiBr_6$, 0.01M and 0.05M thin films. In Figure 4d, the investigated samples' VBM, CBM, and vacuum energy levels are depicted relative to their respective E_F. A band diagram with absolute values is shown in **Figure S11**. Furthermore, the energetic difference between E_F and CBM decreases from $Cs_2AgBiBr_6$ towards 0.05M, as observable in Figure 4d.

To further elucidate the surface-passivating effects of the mixed 2D/3D phase, we investigated the 2D modifications' effects on the photoluminescence (PL) of the perovskite thin films. Steady-state PL of thin films is depicted in Figure 4e. Pure $Cs_2AgBiBr_6$ and the 2D/3D modified samples feature a PL maximum at 673 nm, which is characteristic of $Cs_2AgBiBr_6$, usually recognized as the indirect band gap slow emission from the excited state that is responsible for the shallow absorption at 650 nm (Figure 3b, inset graph).[69] The absolute intensity of this emission peak decreases with increasing thickness of the 2D modification. We assume this behavior to be caused by the introduction of new oscillation modes, originating from the mixed 2D/3D perovskite, that affect the dynamics of the population of the red-shifted excited state, and therefore enhance the carrier relaxation modes by a non-radiative recombination mechanism. It is important to highlight that the red window of the absorption spectrum is not accountable for the overall optoelectronic performance, but only the high-energy excitonic peak (Figure 3b) significantly contributes to the photo-absorption. The photocurrent of the different solar cells does not decrease but increases, as discussed in a later section of this report. Consequently, a faster dissociation of excited states would also explain suppressed emission and, therefore, improved solar cell efficiency.

Time-resolved PL (TRPL) decay curves are depicted in Figure 4f. To extract information about charge carrier lifetimes, the curves were fitted with the triple exponential function

$I(t) = \sum A_i \exp(-t/\tau_i)$ ($i = 1, 2, 3$)

with A_i being the respective component's amplitude, and τ_i its respective lifetime.[29,76] The extracted parameters are shown in Table S1. While the fast and intermediate lifetimes τ_1 and τ_2 are reported to correspond to trap and surface state emission, the slow component τ_3 allows an estimation of the material's fundamental charge carrier lifetime since it was reported that around 80% of the charge carriers emit via the long-lived recombination process.[29,76] A comparison of τ_3 for $Cs_2AgBiBr_6$ and the 2D/3D modified thin films reveals that τ_3 increases from pure $Cs_2AgBiBr_6$ (40 ns) to 0.01M (59 ns) and 0.05M (182 ns), while it decreases again for 0.1M (165 ns).

However, it is important to note that the relative carrier population of the three recombination processes is unknown. To obtain the correct charge carrier lifetime, the PL quantum yield (PLQY) of the distinct processes must be considered.

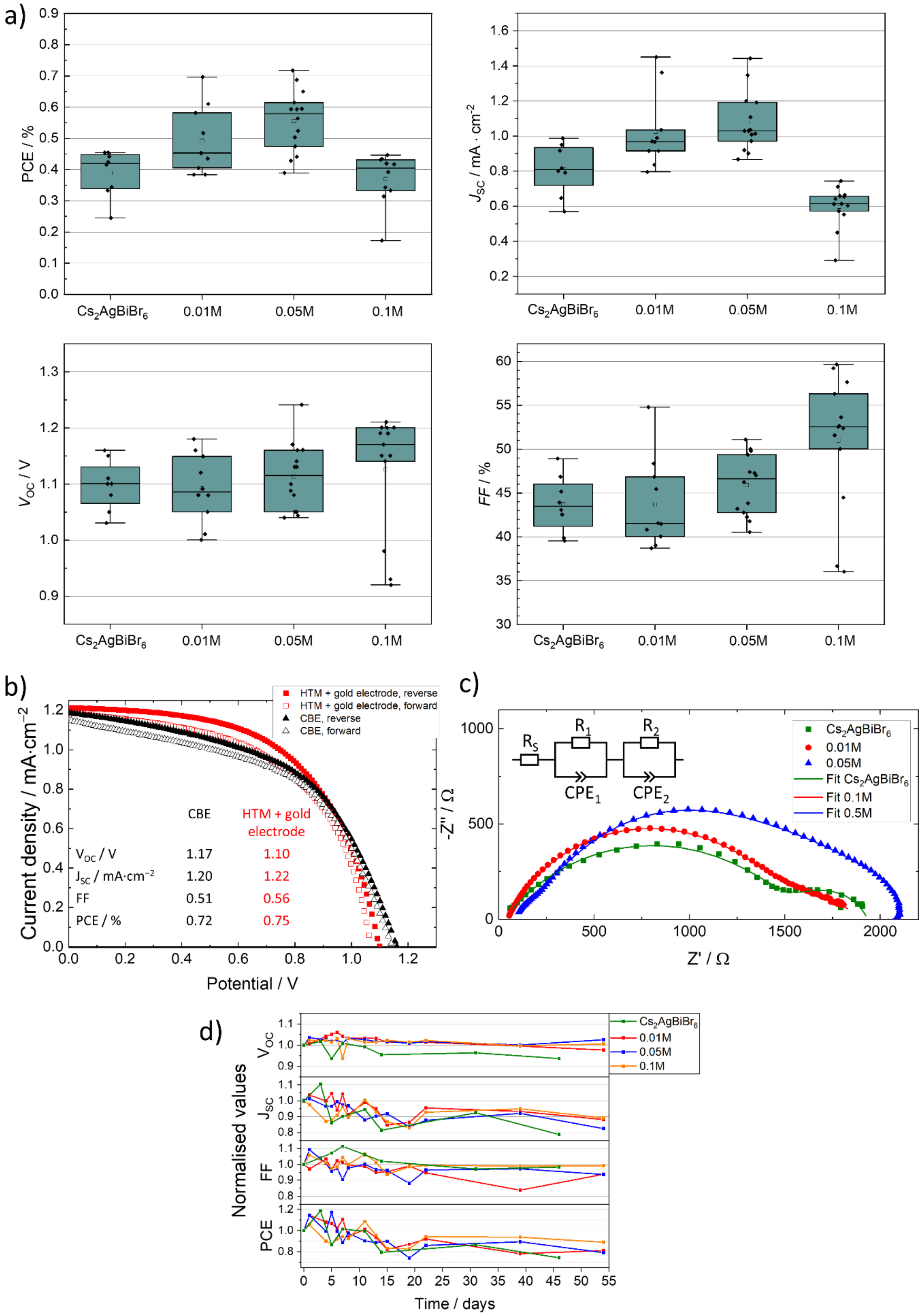

Figure 5. 2D/3D modified $Cs_2AgBiBr_6$ solar cells characterization. a) Statistics on relevant figures of merits for HTM-free solar cells containing a CBE top-electrode. b) *J-V* characteristics for 0.05M modified devices containing either a CBE top-electrode or Spiro-OMeTAD HTM

and gold electrode. c) EIS characterization on pristine and 2D/3D modified $Cs_2AgBiBr_6$ solar cells containing a Spiro-OMeTAD HTM and a gold top-electrode. d) Variations in relevant figures of merit for HTM-free solar cells containing a CBE top-electrode over 54 days of storage in standard laboratory conditions.

The CBEs of this work's HTM-free $Cs_2AgBiBr_6$ solar cells consisted of carbon black powder which was obtained from a pyrolytic process using hazelnut shell waste, *via* a procedure that is described in an earlier work.[77] As described in detail in the Experimental Section, the carbon black was ball-milled in a polyvinylpyrrolidone (PVP) solution in isopropanol for several hours to fabricate a viscous paste which is depicted in Figure S1b. The back electrodes were then deposited onto the perovskite thin films *via* screen-printing and consecutive thermal annealing. PVP was added to the paste to increase its viscosity (rheometric details shown in **Figure S12**) and optimize the screen-printing deposition: while a too-low viscosity leads to smearing of the electrodes directly after their deposition, a too-high viscosity results in agglomerations and inhomogeneities of the electrodes. Reference solar cells were fabricated by first depositing Spiro-OMeTAD on the perovskite thin films *via* spin-coating, followed by electron-beam deposition of gold electrodes. Details of the Spiro-OMeTAD and gold electrode deposition procedures can be found in the Experimental Section.

Current density-voltage (*J*-*V*) curves of the solar cells that were prepared as depicted in Figure S1a were measured under AM 1.5G irradiation. In **Figure 5a**, the parameters of multiple CBE solar cells consisting of pure $Cs_2AgBiBr_6$ as well as of the 2D modified thin films are depicted. The application of a 2D modification of the $Cs_2AgBiBr_6$ perovskite film is expected to suppress the interfacial recombination between the perovskite layer and CBE due to defect passivation.[46,51,52] Also, the band alignment between perovskite and CBE can be improved due to an increased valence band (VB) energy when the 2D modification is applied (Figure 4d). Accordingly, a change in solar cell parameters can be associated with the different treatments of the $Cs_2AgBiBr_6$ thin film. For 0.01M, the average open-circuit voltage (V_{OC}) and fill factor (FF) are close to that of pure $Cs_2AgBiBr_6$ but its short-circuit current density (J_{SC}) is increased, which leads to a 7% improvement of the average PCE compared to $Cs_2AgBiBr_6$. For 0.05M, the average J_{SC}, V_{OC}, and FF are further enhanced in comparison with pure $Cs_2AgBiBr_6$ and 0.01M, and the average and record PCEs of 0.05M improve by 38% and 57%, respectively, compared to $Cs_2AgBiBr_6$. Using this modification, we also achieved a record V_{OC} of 1.25 V within all CBE solar cells in this work. The enhanced PCEs of 0.05M solar cells stem from the improved valence band alignment towards the CBE which results in improved J_{SC} as well as the formation of a high-lying CBM, creating an energy barrier that suppresses recombination at the perovskite CBE interface, thus enhancing the CBE's selectivity (see Figure 4d). However, the PCE does not further improve with increasing concentration of the BABr solution: Although the average V_{OC} of 0.1M is further enhanced, their J_{SC} strongly decreases due to the insulating character of the organic double layers in between the large number of 2D layers (see Figure 3a). Furthermore, we compared the performances of the HTM-free CBE solar cells with solar cells consisting of Spiro-OMeTAD and gold. The *J*-*V* characteristics of the respective best-performing solar cells for 0.05M are shown in Figure 5b. While the CBE device achieves a higher V_{OC}, the gold electrode device possesses a better FF. We assume the origin of the high V_{OC} to be attributed to the presence of an electric dipole at the perovskite/CBE interface, as we reported on devices with similar CBE solar cells, in a previous work.[77] Surprisingly, the current densities of both electrodes show almost no differences although the CBE's resistivity is six orders of magnitude higher than that of gold. This leads to comparable PCEs and J_{SC}s for the record devices of both top electrode types, implying that the CBE is not the efficiency-hampering bottleneck for those devices.

We performed electrochemical impedance spectroscopy (EIS) on $Cs_2AgBiBr_6$, 0.01M, and 0.05M solar cells, shown in Figure 5c, to analyze the origin of the increased solar cell performances. The CBEs possess a resistivity ρ of 5.1 mΩ·m (for comparison: $\rho_{gold} = 2.20 \cdot 10^{-5}$ mΩ·m) obtained by measuring the sheet resistance of carbon electrodes that were deposited on insulating glass with a four-point-probe setup. Therefore, to obtain reliable and reproducible impedance spectra, we compared only $Cs_2AgBiBr_6$, 0.01M, and 0.05M devices with HTM and gold electrodes since the high resistivity of the carbon electrodes strongly affected the impedance spectra in the low-frequency regions. We applied an equivalent circuit model (ECM), depicted in Figure 5c, that allows us to determine the recombination resistance as well as the selective contact resistance.[43] The former is expected to increase with increasing BABr concentration due to the defect-passivating properties of capping 2D modifications, whereas the latter is expected to decrease due to improved band alignment, as depicted in the scheme of Figure 1, and in Figure 4d. The ECM consists of a resistor R_S representing the resistance of the wires, contacts, and electrodes, one resistor R_1//constant phase element (CPE_1) circuit to model the selective contacts for low frequencies, as well as an R_2//CPE_2 circuit representing the interfacial recombination at high frequencies.[43] Parameters obtained by fitting the ECMs to the respective impedance spectra are shown in Table S2 in the Supporting Information. With increasing thickness of the 2D modification, the interfacial recombination resistance R_2 is increasing from 367 Ω ($Cs_2AgBiBr_6$) to 610 Ω (0.01M) and 1760 Ω (0.05M), in line with a strongly decreasing rate of recombination. These results agree with increased carrier lifetimes obtained from TRPL analyses we performed on the respective perovskite thin films and are also supported by the enhanced V_{OC} that causes the improvement of the shunt resistance values leading to FF value optimization of the 0.05M solar cells. Additionally, the decreasing selective contact resistance R_1 with increasing 2D modification thickness corresponds with an enhanced charge carrier injection into the selective contacts from the perovskite layer. For the $Cs_2AgBiBr_6$ solar cells (1536 Ω) it is the largest and it reduces for 0.01M (1284 Ω) and 0.05M (409 Ω). This behavior results from the improved band alignment and selectivity of the 2D/3D modified thin films (Figure 4d).

Since the 2D modification increased the thin films' hydrophobicity and passivated the material, we evaluated the evolution of solar cell parameters within several weeks, as shown in Figure 5d. While the $Cs_2AgBiBr_6$ solar cells already possess a long device lifetime, the 2D/3D modification further enhanced their longevity. Especially the 0.1M devices retained close to 90% of their initial efficiency after 54 days. Their high conversion of 3D perovskite into 2D phases provides the best protection against efficiency losses in 0.1M, which results in the highest long-term stability. However, since the PCEs in Figure 5d are normalized values, the 0.1M solar cells still on average possess the lowest efficiencies of all solar cells discussed in this report.

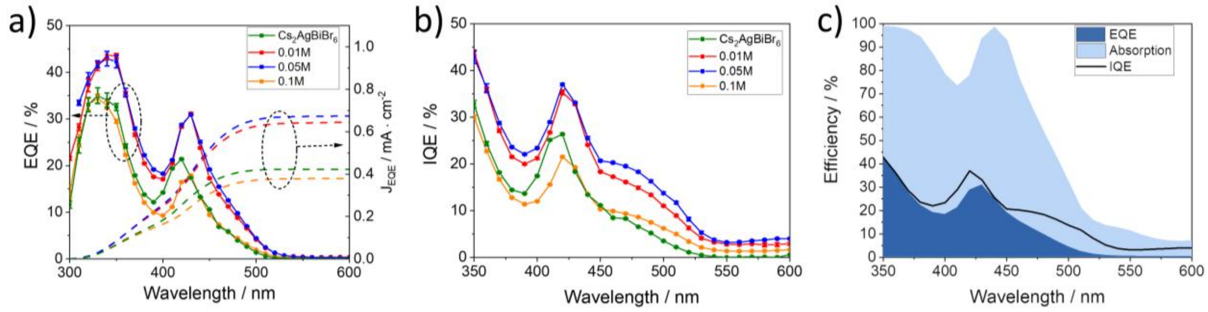

Figure 6. Quantum efficiencies of 2D/3D modified $Cs_2AgBiBr_6$ solar cells with CBE. a) EQE (left y-axis, squares connected by solid curves) and integrated current densities (right y-axis, dotted curves). b) IQE, calculated using absorption spectra from Figure 3b. c) EQE (dark blue), IQE (light blue), and absorption (black curve) of 0.05M in direct comparison.

To investigate the origin of the increased J_{SC} of the 0.01M and 0.05M solar cells, we performed external quantum efficiency (EQE) determination, as shown in **Figure 6a**. The EQE of 0.01M and 0.05M feature an absolute maximum at around 340 nm of ~43% and a local maximum at around 440 nm of ~32% and therefore possess close similarity to the absorbance spectra (Figure 3b) in their shape. In comparison, the spectra of $Cs_2AgBiBr_6$ possess a similar shape but their EQE is reduced by around 10% throughout the entire spectrum which is in accordance with the reduced J_{SC} of $Cs_2AgBiBr_6$ compared to 0.01M, and 0.05M solar cells (Figure 5a). At the 440 nm maximum, the EQE of all 2D modified solar cells is slightly red-shifted in comparison to the $Cs_2AgBiBr_6$. Furthermore, the internal quantum efficiency (IQE) of the 2D-modified solar cells is drastically increased close to bandgap energies in comparison to $Cs_2AgBiBr_6$ (see Figure 6b). This behavior corresponds to an enhanced charge carrier extraction close to the band edges. It can best be observed by comparing $Cs_2AgBiBr_6$ and 0.1M (see Figure 6b): while $Cs_2AgBiBr_6$ shows higher IQE at the 440 nm maximum, the IQE of 0.1M is higher in the region between 450 and 520 nm, close to the bandgap. To compare the different behavior of IQE and EQE at bandgap wavelengths as well as sub-bandgap wavelengths, both are depicted for the 0.05M solar cell in Figure 6c.

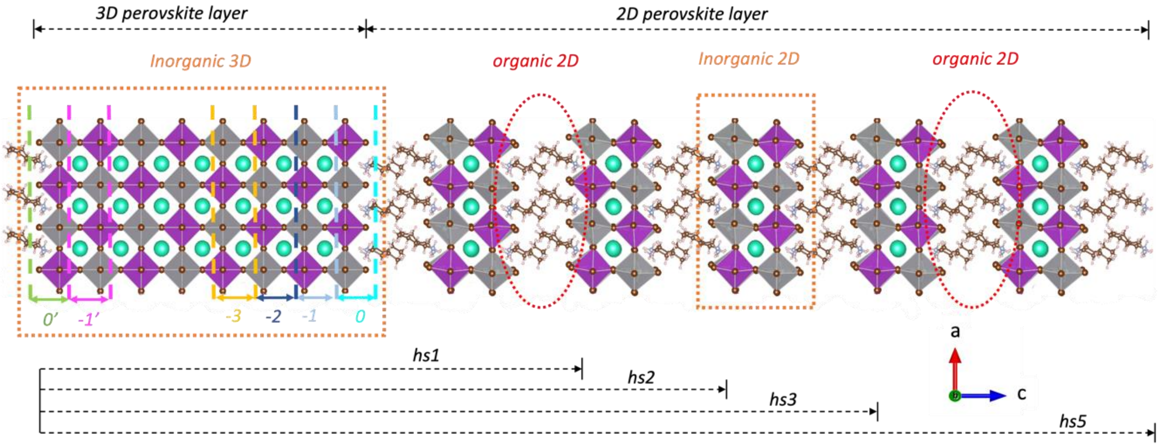

Figure 7. Slab models considered for DFT calculations. Divisions of 3D perovskite layer used to calculate npDOS for respective slabs. Periodic boundary conditions applied along the direction perpendicular to the surface result in the creation of two equivalent 3D/2D interfaces.

The viability of the 2D perovskite phase as an HTM has also been assessed *via* density functional theory (DFT) calculations. To investigate the effect of increasing number of 2D double perovskite stacks we calculated samples consisting of 3D/2D heterostructures made of 8 symmetric layers of 3D cubic double perovskite ($Cs_2AgBiBr_6$) slab and a 2D ($(BA)_2CsAgBiBr_7$)) capping layer with growing number of layers (**Figure 7** - see supporting information Table S3 for detailed structural information). In particular, we considered four heterostructures containing 1, 2, 3, and 5 2D layers, dubbed hs1, hs2, hs3 and hs5, respectively. **Figure 8** presents the density of states (DOS) projected (pDOS) on the 3D, and organic and inorganic sublattices of 2D domains of the hs1 heterostructure. One notices that the VBM and close-by energy states are related to the 3D and the inorganic sublattice of the 2D double perovskites, which is in agreement with previous studies.[23,46,58,78] Similar results are found for the other heterostructures (**Figure S13).**

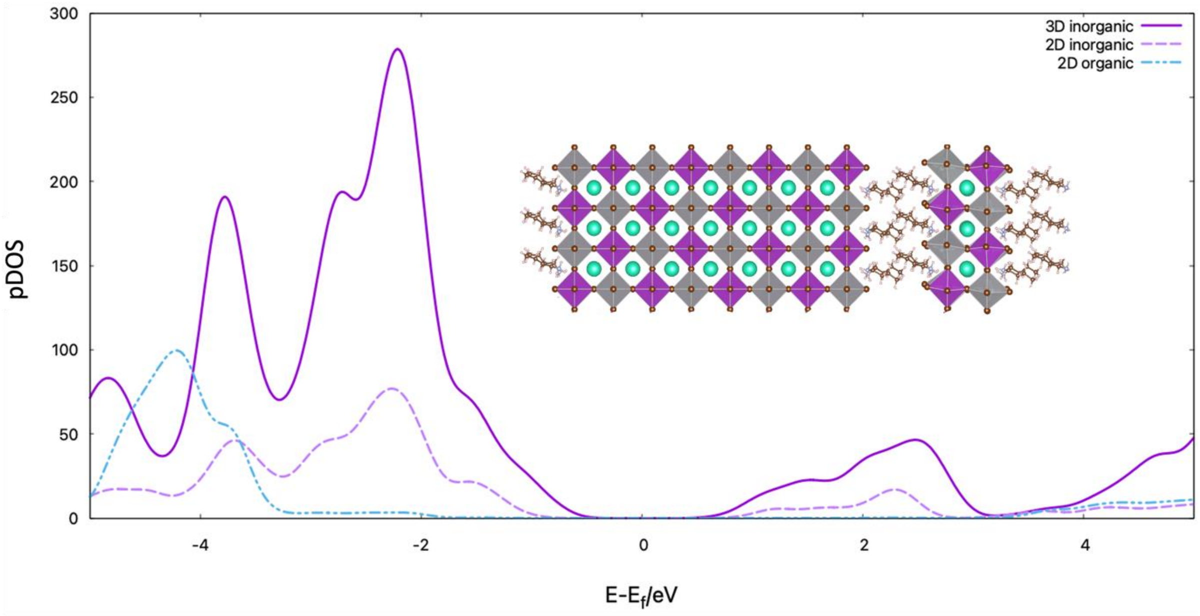

Figure 8. pDOS calculated for 3D/2D hs1.

To identify the microscopic origin of the enhanced charge extraction revealed by the increased IQE with BABr concentration up to 0.05 M, we computed the contribution of the various layers of Figure 7 of the 3D slab to the density of states (see **Figure S14**). This contribution, expressed in percentage and denominated *normalized* pDOS (npDOS), is obtained by dividing pDOS relative to one 3D layer by (total) DOS and multiplying by 100. npDOS is set to zero in the region of the bandgap. One sees that for the single 2D bilayer (hs1), the contribution of the interface 3D layer (0) to the DOS at VBM and closer energies is the lowest among all the layers of the $Cs_2AgBiBr_6$ computational slab, with the largest contribution arising from the bulk-like layers (−3). This implies that for the hs1 sample, one has little probability of finding holes at the 3D/2D interface and their extraction is inefficient. The picture changes with the increase of the thickness of the 2D slab, with the contribution of the interface layer to the VBM growing steadily from 3 to, 10, to 16, to 26% for hs1, hs2, hs3, and hs5, respectively. A similar effect of a thicker 2D layer is observed up to 0.7 eV below the VBM. This increase in the contribution of the interface layer to VBM means that thermalized holes are closer to the interface, which makes their extraction easier as revealed in the experiments. We attribute to this phenomenon the increase of the IQE close to the bandgap energy (see Figure 6b).

However, experimental IQE shows a maximum at the bandgap for the 0.05M solar cells. We attribute this phenomenon to two additional effects of the thickness of the 2D capping layer. First, the resistance of the 2D capping layer increases with its thickness, balancing the beneficial effect of the heterostructure in attracting holes at the interface. Moreover, 2D layer capping has also the effect of increasing the contribution of the interface 3D layer in the CBM (**Figure S15**), i.e., attracting electrons in the conduction band toward a region of higher concentration of holes. Thus, a longer residence time of holes at the interface due to the longer extraction time of the thicker 2D layer favors their recombination with electrons also present in this region. This leads to a reduction of the current density and, henceforth, PCE.

Experimental results from TRPL (Figure 4f) and EIS (Figure 5c) suggest that the 2D layers passivate defects and, here, we investigate the microscopic origin of this phenomenon. We considered the three most likely defects in bulk $Cs_2AgBiBr_6$:[79–83] bismuth antisite, and bismuth and bromide vacancies: Ag_{Bi}'', V_{Bi}''', and $V_{Br}^{\bullet}$, following the Kröger-Vink notation. We computed the relative energy of these defects as a function of their position along the slab (**Figure 9 a-c**) for the 2D capping at various thicknesses. First and foremost, we notice that all defects (encircled in pink) are more stable when moved away from the interface layer. In other words, the effect of 2D capping is preventing any accumulation of defects at the $Cs_2AgBiBr_6$ surface, where, as shown before, we have an accumulation of holes and electrons and defects can promote recombination. Our simulations suggest that the *passivation* effect of 2D capping is, indeed, not passivation in the usual sense: here, the presence of 2D layers prevents the accumulation of defects at the 3D surface/interface. Concerning defect *passivation*, the thickness of the slab does not play any major role: we observe similar energy of defects vs position in the 3D slab for all heterostructures, regardless of the thickness of the 2D layer.
To further investigate the effect of defect passivation of the 2D capping, we performed analogous calculations for a 3D/Spiro-OMeTAD interface model. We also computed the relative energetics of $V_{Br}^{\bullet}$, and Ag_{Bi}'' defects as functions of position. At a variance with the 3D/2D system, we noticed that with Spiro-OMeTAD both defects are attracted to the interface layer (see Figure S16 in the supporting information). Even in the absence of any defect at the perovskite interface layer, a visual inspection of the minimum energy configuration clearly shows a more pronounced and prolonged (farther from the interface) distortion of the perovskite lattice with respect to the 2D/3D sample (compare figures S17 and S18). It is well known that tilting of $[AgBr_6]^{5-}$ and $[BiBr_6]^{3-}$ octahedra in the case of double perovskites affects its electronic structure and consequently the electronic properties.[24] Indeed, the pDOS of the

interface layer of the defect-free 3D/Spiro-OMeTAD system (Figure S19) shows some orbitals with energies deeper in the bandgap with respect to the 2D/3D case. These states can either result in trap-assisted recombination or simply slow down carrier dynamics. This effect is enhanced when $V_{Br}^{\bullet}$, and $Ag_{Bi}^{''}$ defects are accumulated at the 3D/Spiro-OMeTAD interface, according to the driving force discussed above. This is illustrated by comparing the pDOS of the interface layer of the pristine and defected 3D/Spiro-OMeTAD system (Figure S20), which shows additional states due to the defects appearing at the bottom of the CB for both types of defects.

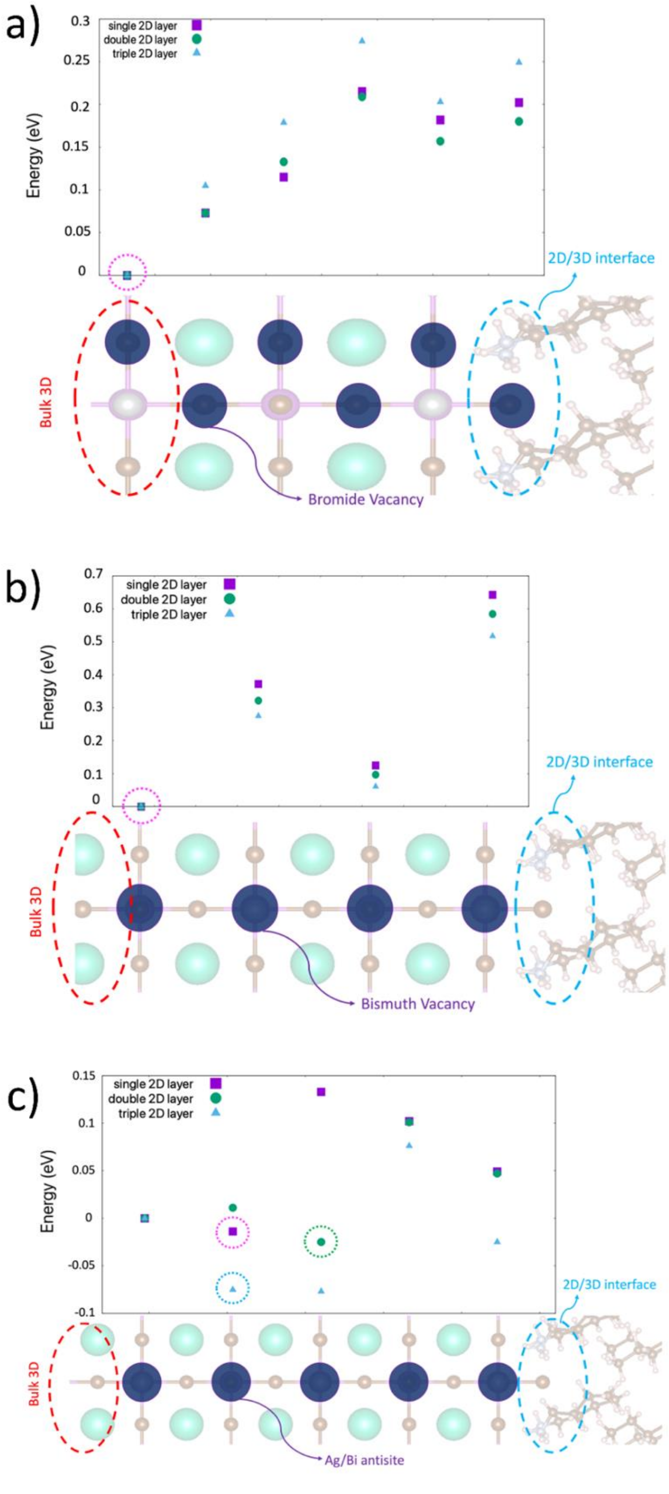

Figure 9. Energy vs position of a) bromide vacancy ($V_{Br}^{\bullet}$), b) Bismuth vacancy (V_{Bi}'''), and c) Antisite (Ag_{Bi}'') of hs1, hs2, and hs3. Dashed circles around symbols denote the state corresponding to the minimum energy defect position. Energies are arbitrarily shifted so that the value in the bulk position is zero. In each panel is reported a cartoon illustrating the portion of the 3D/2D computational sample illustrating the position of the corresponding defect.

3. Conclusion

In this work, we present the fabrication of low-cost HTM-free 2D/3D-modified double perovskite solar cells *via* a treatment of $Cs_2AgBiBr_6$ thin films with n-butylammonium bromide solution in isopropanol, followed by the deposition of electrodes consisting of carbon black from up-cycled biowaste. The presence of the 2D/3D modification, consisting mainly of $(BA)_2CsAgBiBr_7$ bilayers, is experimentally confirmed, and its thickness is shown to depend on the concentration of the BABr solution. Using a combination of XPS, and KPFM, we provide a band diagram, showing an improved valence band alignment between $Cs_2AgBiBr_6$ and the CBE for 2D/3D modified solar cells as well as a strongly increased CBM, leading to enhanced selectivity. Both effects are further confirmed *via* electrochemical characterization and result in improved J_{SC}, V_{OC}, FF, and PCE for HTM-free 2D/3D $Cs_2AgBiBr_6$ solar cells that were treated with 0.05 M BABr solution. DFT calculations, that simulate various numbers of $(BA)_2CsAgBiBr_7$ bilayers which are capping 3D $Cs_2AgBiBr_6$, reveal that the presence of 2D perovskite increases the 3D phase's DOS for holes at the 2D/3D interface and, therefore, enhances the hole extraction probability. The calculations are supported by an improved IQE for 2D/3D-modified solar cells close to their band edge.

This work demonstrates how the application of a 2D/3D modification enhances the PCE of HTM-free $Cs_2AgBiBr_6$ solar cells. The absence of an HTM and the substitution of the metal electrode not only strongly reduce the device costs, but the application of the carbon electrode from up-cycled biowaste also represents a path towards "green" PV. Furthermore, the drawbacks of low selectivity and weak band alignment for HTM-free photovoltaics are mitigated by the formation of the 2D/3D mixed perovskite phase. Although our solar cells possess relatively low PCEs, which is a common problem for this material,[38,41–49] there are promising reports of highly improved $Cs_2AgBiBr_6$, i.e. by hydrogenating the material, that will benefit from applying our approach to further boost such technology.[84]

4. Experimental Section

Fabrication of 2D modified $Cs_2AgBiBr_6$ thin films. The preparation of $Cs_2AgBiBr_6$ thin films as well as their 2D modification were entirely performed in an argon-filled glovebox. First, $Cs_2AgBiBr_6$ powder, which was synthesized as described in previous work,[30] was dissolved in dimethyl sulfoxide (99.7+%, thermos scientific) to create a 0.5 mol/L precursor solution. The solution was stirred until the powder was fully dissolved. To deposit the $Cs_2AgBiBr_6$ thin film, a substrate (2 x 2 cm^2) was mounted onto a spin-coater, precursor solution (50 µL) was evenly spread across the substrate, and the substrate was rotated at 4000 rpm for 40 s (3 s acceleration time). Immediately after the spin-coating process, the substrate was transferred to a pre-heated 285 °C hot plate and annealed for 5 minutes. To prepare the 2D modification, we adapted the synthesis route from Sirtl *et al*.[46] The room-temperature $Cs_2AgBiBr_6$ thin films were again mounted onto a spin-coater, then n-butylammonium bromide (Aldrich) solution (100 µL, 0.01/0.05/0.1 mol/L in isopropanol) were evenly spread across the thin films, and they were rotated at 4000 rpm for 40 s. Afterward, the thin films were left to dry in the glovebox overnight.

Preparation of solar cells. FTO covered glass substrates were etched as depicted in Figure S1a and cleaned by consecutive ultrasonication in demineralized water, acetone, and isopropanol for 15 minutes each. Then, the substrates were UV-ozone treated for 15 minutes and mounted on a spin-coater under ambient atmosphere. They were covered with commercial compact TiO_2 precursor solution (70 µL, Solaronix), rotated at 5000 rpm for 30 s, and annealed for 1 h at 550°C in air. For the preparation of the mesoporous TiO_2 layer, the substrates were again UV-ozone cleaned for 15 minutes and mounted on a spin-coater. They were covered with diluted (1:5 abs. ethanol) commercial mesoporous TiO_2 precursor solution (100 µL, Solaronix), rotated at 5000 rpm for 30 s, and then annealed at 475 °C for 30 min in air. Before the deposition of the $Cs_2AgBiBr_6$, the substrates were heated at 400 °C for 30 min to release water encapsulated in the TiO_2 scaffold. The substrates were then transferred into an argon-filled glove box and the perovskite layers were deposited as described above.

Deposition of CBE. The CBE precursor paste was prepared by first dissolving PVP (70 mg) in of isopropanol (2 mL). The solution was vigorously stirred overnight until the PVP was fully dissolved. Then, the viscous solution was mixed with carbon black (100 mg) that was synthesized *via* a process analogous to the one described in our previous work.[77] The mixture was ball-milled at 250 rpm for 3 h using two stainless steel balls (1 cm diameter) to create a homogeneous, viscous carbon paste (Figure S1b). The CBEs were deposited *via* screen-printing (mesh size 80T) and then annealed at 100 °C for 1 h.

Deposition of HTM and gold electrode. The HTM for the reference devices was deposited according to the literature.[46] To prepare the HTM precursor solution, Spiro-OMeTAD (73 mg) was dissolved in chlorobenzene (1 mL) in an argon-filled glove box. To this solution, 4-tert-butylpyridine (10 µL) and lithium bis(trifluoromethanesulfonyl)imide solution (30 µL, 170 mg dissolved in 1 mL acetonitrile) was added. The solution was spin-coated onto the perovskite layer at 1500 rpm for 45 s. Gold electrodes with 60 nm thickness were deposited *via* electron-beam physical vapor deposition.

Characterization. Grazing Incidence x-ray diffraction (GIXRD) measurements were performed with a PANalytical B.V. X'Pert Pro diffractometer using Cu Kα1 radiation. The instrument was operated at 40 kV and 40 mA, the step size was 0.05°, and the scan speed was 0.014° s^{-1}. The diffraction patterns were measured along the 2θ axis with a grazing incidence of $\omega = 0.5°$. Thin film absorption spectra were measured using a two-ray setup with a UVIKON XS from Schott Instruments. Contact angles were conducted with an OCA 20 from Dataphysics Instruments GmbH using demineralized water. Scanning electron microscopy (SEM) images were taken using a GeminiSEM 560 from Zeiss at a working potential of 1 kV. High-resolution transmission electron microscopy (HRTEM) images were taken using a Talos F200X from Thermo Scientific (Eindhoven, Netherlands). The analysis was performed at an acceleration voltage of 200 kV. Energy-dispersive x-ray spectroscopy (EDX) was performed with a 4-quadrant EDX detector in scanning transmission electron microscopy (STEM) mode. Further instrument details as well as a description of the sample preparation are shown in the Supporting Information. x-ray photoelectron spectroscopy (XPS) was performed with a PHI 5000 VersaProbe II Scanning ESCA Microprobe (Physical Electronics) with monochromatized Al Kα x-ray source in high power mode (beam size 1300 µm x 100 µm, x-ray power: 100 W). Time steps of 50 ms, a step size of 0.2 eV, and an analyzer pass energy of 46.95 eV were used for measuring the detail spectra. For every detailed region, 30 sweeps, or a P/N ratio equal to 180, were set. The sample surface was charge neutralized with slow electrons and argon ions, and the pressure was in the range from 10^{-7} Pa to 10^{-6} Pa during the measurement. Data analysis was performed using the CasaXPS software.[85] Diffuse reflectance infrared Fourier transform spectroscopy (DRIFT) was performed with a Bruker alpha. The spectra were recorded in a range of 400-4000 cm^{-1} with a resolution of 2 cm^{-1}. Atomic force microscopy (AFM) and Kelvin probe force microscopy (KPFM) were carried out using an AIST NT Vacuscope 1000 microscope operated below $5 \cdot 10^{-6}$ mbar with SPARK 350 Pt-coated AFM probes excited at the resonant frequency of around 300 kHz. An amplitude of 8.5 nm was chosen for the non-contact morphology scans in AC-mode operation. The work function was obtained by measuring the contact potential difference between the probe and sample *via* FM-KPFM at an AC amplitude of 2 V at around 1 kHz. The probe work function was referenced by obtaining the contact potential difference of the probe to a freshly cleaved highly oriented pyrolytic graphite (ZYB, MikroMasch) with a known work function of 4.6 eV before and after each measurement. Linear sweep voltammetry (J-V curves) was conducted with an IviumStat potentiostat from Ivium Technologies. Solar cells were measured with a rate of 0.05 $V \cdot s^{-1}$. For irradiation, an LS0160 solar simulator from LOT-Oriel with an LSB521U 150 W xenon high-pressure arc lamp and an LSZ189 AM1.5 filter (both LOT-Oriel) was used. The power density was calibrated to 100 $mW \cdot cm^{-2}$ using an ML-020VM pyranometer from ECO Instruments. All measured solar cells were masked (3 x 3 mm²). Electrochemical impedance spectroscopy (EIS) was performed with an SP-50e potentiostat from BioLogic. The spectra were taken at frequencies from 10 Hz to 1 MHz and were analyzed using the software RelaxIS (rhd instruments). The microphotoluminescence spectra were collected at room temperature on a LabRAM HR Evolution spectrometer (Horiba Jobin Yvon) equipped with an Olympus BXFM-ILHS confocal microscope working in backscattering geometry and Syncerity OE detector. Solid-state Cobolt Blues 25 laser was used as the excitation line at 473 nm with a beam power of 400 µW. Measurements were performed over the spectral range 500-850 nm and the signal was acquired with a 100× objective (NA = 0.9). The diameter of the confocal hole was 500 µm, and the diffraction grating was 300 lines/mm. For each spectrum, 5 acquisitions with an accumulation time of 1 s each were averaged. Spectra were smoothed and background-corrected where necessary. The fluorescence decay curves and fluorescence map measurements were performed on a MicroTime 200 confocal microscope (PicoQuant). As an excitation source, a 402 nm pulsed laser diode was used. The beam was directed *via* a dichroic mirror (Chroma ZT405rdc) into the Olympus IX71 microscope. Simultaneously, fluorescence emission passed the dichroic and was focused on a pinhole (size 30 µm). After the pinhole, the fluorescence light passed the 600 nm longpass filter (Thorlabs FEL0600) and was focused on the SPAD detector (Excelitas Technologies SPCM CD 3516 H). All measurements were performed using the SymPhoTime Software (PicoQuant). External quantum efficiency (EQE) measurements were conducted using a LSB551 1000 W xenon arc lamp, and a SpectraPro 2300i (Action) Monochromator. The spectra were measured using an IviumStat potentiostat from Ivium Technologies. Calibration on the incident photon number was done using an FDS100 silicon photodiode from Thorlabs. The internal quantum efficiency (IQE) was calculated by dividing the EQE by the absorption of the respective thin films.

Simulations. Three computational samples were considered ; sample 1) An eight-layer thick slab of $Cs_2AgBiBr_6$ oriented along the (001) crystallographic direction was prepared, and its geometry was optimized. On this, we deposited slabs of $(BA)_2AgBiBr_7$ with various layers of the material. Simulations are performed within periodic boundary conditions (PBC) and the 3D and 2D slabs are combined so that the two 3D/2D interfaces are symmetric and there is no induced dipole moment (see **Figure S15** in the Supporting Information); slabs 2 & 3) The thickness and the orientation of the $Cs_2AgBiBr_6$ slab along (001) direction was retained, however, the width was doubled along the (100) and (010) directions and its geometry was optimized. On this slab, we deposited the Spiro-OMeTAD molecule. While the $Cs_2AgBiBr_6$ slab is of the same dimensions for samples 2 and 3, the orientation of the HTM molecule differs.

This approach is considered as no experimental data are available on the binding characteristics of Spiro-OMeTAD to DP surface. We refer to these different orientations as the different binding modes (see Figure S16). Furthermore, one can have different surface/interface terminations in a crystallite in experimental samples. On the contrary, all our samples are symmetrically terminated. This is because computational samples are much smaller than experimental ones (few nanometers vs hundreds of nanometers to micrometers) and systematic asymmetries associated with different terminations likely, possibly introducing a dipole moment in the slab, may induce large electric fields. This likely induces artifacts in the computational results. Density functional calculations were performed within the Perdew–Burke–Ernzerhof generalized gradient approximation. Simulations were performed with the VASP code. Kohn-Sham orbitals were expanded on a planewave basis set with an energy cutoff of 400eV. The interaction between valence electron and nuclei plus core electron was described within the projector augmented-wave formalism.[86,87] For the computational sample 1, the Brillouin zone has been sampled with 4x4x1 K-points,[88] the latter figure referring to the (001) direction. For the other two computational samples, because of their larger size in the surface plane necessary to accommodate Spiro-OMeTAD, we used Γ-point sampling only. The suitability of this setup was validated by checking the convergence of total energy, bandgap, and atomic forces with respect to the parameters listed above.

Supporting Information

Supporting Information is available from the Wiley Online Library or from the author.

Acknowledgements

T.G. would like to acknowledge the financial support of the European Research Council through the ERC StG project JANUS BI (grant agreement no. [101041229]). P.P., J.C., P.P., G.D. and D. P. thank the ENSEMBLE^3 Project (MAB/2020/14) which is carried out within the International Research Agendas Programme (IRAP) of the Foundation for Polish Science co-financed by the European Union under the European Regional Development Fund and Teaming Horizon 2020 programme of the European Commission.

References

[1] F. Perera, K. Nadeau, *N. Engl. J. Med.* **2022**, *386*, 2303.
[2] M. Höök, X. Tang, *Energy Policy* **2013**, *52*, 797.
[3] N. L. Panwar, S. C. Kaushik, S. Kothari, *Renew. Sustain. Energy Rev.* **2011**, *15*, 1513.

[4] A. W. Faridi, M. Imran, G. H. Tariq, S. Ullah, S. F. Noor, S. Ansar, F. Sher, *Ind. Eng. Chem. Res.* **2023**, *62*, 4494.

[5] Q. Jiang, Z. Chu, P. Wang, X. Yang, H. Liu, Y. Wang, Z. Yin, J. Wu, X. Zhang, J. You, *Adv. Mater.* **2017**, *29*, 1.

[6] J. Guo, B. Wang, D. Lu, T. Wang, T. Liu, R. Wang, X. Dong, T. Zhou, N. Zheng, Q. Fu, Z. Xie, X. Wan, G. Xing, Y. Chen, Y. Liu, *Adv. Mater.* **2023**, *35*, 1.

[7] B. Li, Y. Zhang, L. Zhang, L. Yin, *J. Power Sources* **2017**, *360*, 11.

[8] N. De Marco, H. Zhou, Q. Chen, P. Sun, Z. Liu, L. Meng, E. P. Yao, Y. Liu, A. Schiffer, Y. Yang, *Nano Lett.* **2016**, *16*, 1009.

[9] D. W. DeQuilettes, S. M. Vorpahl, S. D. Stranks, H. Nagaoka, G. E. Eperon, M. E. Ziffer, H. J. Snaith, D. S. Ginger, *Science (80-.).* **2015**, *348*, 683.

[10] S. H. Turren-Cruz, M. Saliba, M. T. Mayer, H. Juárez-Santiesteban, X. Mathew, L. Nienhaus, W. Tress, M. P. Erodici, M. J. Sher, M. G. Bawendi, M. Grätzel, A. Abate, A. Hagfeldt, J. P. Correa-Baena, *Energy Environ. Sci.* **2018**, *11*, 78.

[11] H. Oga, A. Saeki, Y. Ogomi, S. Hayase, S. Seki, *J. Am. Chem. Soc.* **2014**, *136*, 13818.

[12] W. J. Yin, T. Shi, Y. Yan, *Appl. Phys. Lett.* **2014**, *104*, DOI 10.1063/1.4864778.

[13] R. Prasanna, A. Gold-Parker, T. Leijtens, B. Conings, A. Babayigit, H. G. Boyen, M. F. Toney, M. D. McGehee, *J. Am. Chem. Soc.* **2017**, *139*, 11117.

[14] S. A. Kulkarni, T. Baikie, P. P. Boix, N. Yantara, N. Mathews, S. Mhaisalkar, *J. Mater. Chem. A* **2014**, *2*, 9221.

[15] K. L. Wang, Y. H. Zhou, Y. H. Lou, Z. K. Wang, *Chem. Sci.* **2021**, *12*, 11936.

[16] C. Polyzoidis, K. Rogdakis, E. Kymakis, *Adv. Energy Mater.* **2021**, *11*, 1.

[17] X. He, J. Chen, X. Ren, L. Zhang, Y. Liu, J. Feng, J. Fang, K. Zhao, S. F. Liu, *Adv. Mater.* **2021**, *33*, 2100770.

[18] Y. Zhao, F. Ma, Z. Qu, S. Yu, T. Shen, H. X. Deng, X. Chu, X. Peng, Y. Yuan, X. Zhang, J. You, *Science (80-.).* **2022**, *377*, 531.

[19] K. L. Wang, H. Lu, M. Li, C. H. Chen, D. Bo Zhang, J. Chen, J. J. Wu, Y. H. Zhou, X. Q. Wang, Z. H. Su, Y. R. Shi, Q. S. Tian, Y. X. Ni, X. Y. Gao, S. M. Zakeeruddin, M. Grätzel, Z. K. Wang, L. S. Liao, *Adv. Mater.* **2023**, *35*, 1.

[20] A. Babayigit, A. Ethirajan, M. Muller, B. Conings, *Nat. Mater.* **2016**, *15*, 247.

[21] C. Chen, S. Cheng, L. Cheng, Z. Wang, *Adv. Energy Mater.* **2023**, 2204144.

[22] M. T. Sirtl, M. Armer, L. K. Reb, R. Hooijer, P. Dörflinger, M. A. Scheel, K. Tvingstedt, P. Rieder, N. Glück, P. Pandit, S. V. Roth, P. Müller-Buschbaum, V. Dyakonov, T. Bein, *ACS Appl. Energy Mater.* **2020**, *3*, 11597.

[23] E. T. McClure, M. R. Ball, W. Windl, P. M. Woodward, *Chem. Mater.* **2016**, *28*, 1348.

[24] H. Lei, D. Hardy, F. Gao, *Adv. Funct. Mater.* **2021**, *31*, DOI 10.1002/adfm.202105898.

[25] E. Greul, M. L. Petrus, A. Binek, P. Docampo, T. Bein, *J. Mater. Chem. A* **2017**, *5*, 19972.

[26] R. Wang, H. Li, H. Sun, *Encycl. Environ. Heal.* **2019**, 415.

[27] R. L. Z. Hoye, L. Eyre, F. Wei, F. Brivio, A. Sadhanala, S. Sun, W. Li, K. H. L. Zhang, J. L. MacManus-Driscoll, P. D. Bristowe, R. H. Friend, A. K. Cheetham, F. Deschler, *Adv. Mater. Interfaces* **2018**, *5*, 1800464.

[28] Z. Li, S. P. Senanayak, L. Dai, G. Kusch, R. Shivanna, Y. Zhang, D. Pradhan, J. Ye, Y. Huang, H. Sirringhaus, R. A. Oliver, N. C. Greenham, R. H. Friend, R. L. Z. Hoye, *Adv. Funct. Mater.* **2021**, *31*, 2104981.

[29] A. H. Slavney, T. Hu, A. M. Lindenberg, H. I. Karunadasa, *J. Am. Chem. Soc.* **2016**, *138*, 2138.

[30] F. Schmitz, K. Guo, J. Horn, R. Sorrentino, G. Conforto, F. Lamberti, R. Brescia, F. Drago, M. Prato, Z. He, U. Giovanella, F. Cacialli, D. Schlettwein, D. Meggiolaro, T. Gatti, *J. Phys. Chem. Lett.* **2020**, *11*, 8893.

[31] R. Kentsch, M. Scholz, J. Horn, D. Schlettwein, K. Oum, T. Lenzer, *J. Phys. Chem. C* **2018**, *122*, 25940.

[32] F. Igbari, R. Wang, Z. K. Wang, X. J. Ma, Q. Wang, K. L. Wang, Y. Zhang, L. S. Liao, Y. Yang, *Nano Lett.* **2019**, *19*, 2066.

[33] Z. Li, P. Wang, C. Ma, F. Igbari, Y. Kang, K. L. Wang, W. Song, C. Dong, Y. Li, J. Yao, D. Meng, Z. K. Wang, Y. Yang, *J. Am. Chem. Soc.* **2021**, *143*, 2593.

[34] K. Z. Du, W. Meng, X. Wang, Y. Yan, D. B. Mitzi, *Angew. Chemie - Int. Ed.* **2017**, *56*, 8158.

[35] J. A. Steele, P. Puech, M. Keshavarz, R. Yang, S. Banerjee, E. Debroye, C. W. Kim, H. Yuan, N. H. Heo, J. Vanacken, A. Walsh, J. Hofkens, M. B. J. Roeffars, *ACS Nano* **2018**, *12*, 8081.

[36] J. Leveillee, G. Volonakis, F. Giustino, *J. Phys. Chem. Lett.* **2021**, *12*, 4474.

[37] G. Longo, S. Mahesh, L. R. V. Buizza, A. D. Wright, A. J. Ramadan, M. Abdi-Jalebi, P. K. Nayak, L. M. Herz, H. J. Snaith, *ACS Energy Lett.* **2020**, *5*, 2200.

[38] D. Zhao, C. Liang, B. Wang, T. Liu, Q. Wei, K. Wang, H. Gu, S. Wang, S. Mei, G. Xing, *Energy Environ. Mater.* **2022**, *5*, 1317.

[39] N. K. Tailor, S. K. Saini, P. Yadav, M. Kumar, S. Satapathi, *J. Phys. Chem. Lett.* **2023**, *14*, 730.

[40] N. K. Tailor, N. Parikh, P. Yadav, S. Satapathi, *J. Phys. Chem. C* **2022**, *126*, 10199.

[41] L. Zhang, Y. Xu, P. Niu, M. Lyu, H. Lu, J. Zhu, *J. Phys. D. Appl. Phys.* **2023**, *56*, 075501.

[42] M. S. Shadabroo, H. Abdizadeh, M. R. Golobostanfard, *ACS Appl. Energy Mater.* **2021**, *4*, 6797.

[43] N. Daem, J. Dewalque, F. Lang, A. Maho, G. Spronck, C. Henrist, P. Colson, S. D. Stranks, R. Cloots, *Sol. RRL* **2021**, *5*, DOI 10.1002/solr.202100422.

[44] X. Yang, Y. Chen, P. Liu, H. Xiang, W. Wang, R. Ran, W. Zhou, Z. Shao, *Adv. Funct. Mater.* **2020**, *30*, DOI 10.1002/adfm.202001557.

[45] P. Fan, H. Peng, Z. Zheng, Z. Chen, S. Tan, X. Chen, Y.-D. Luo, Z.-H. Su, J.-T. Luo, G.-X. Liang, *Nanomaterials* **2019**, *9*, 1760.

[46] M. T. Sirtl, R. Hooijer, M. Armer, F. G. Ebadi, M. Mohammadi, C. Maheu, A. Weis, B. T. van Gorkom, S. Häringer, R. A. J. Janssen, T. Mayer, V. Dyakonov, W. Tress, T. Bein, *Adv. Energy Mater.* **2022**, *12*, 2103215.

[47] A. Yang, L. Zhang, Y. Xu, Q. Wang, M. Lyu, H. Lu, J. Zhu, *J. Mater. Sci. Mater. Electron.* **2022**, *33*, 18758.

[48] H. Peng, P. Fan, Z. Zheng, S. Chen, G. Liang, *ACS Appl. Energy Mater.* **2022**, *5*, 15058.

[49] M. Pantaler, K. T. Cho, V. I. E. Queloz, I. García Benito, C. Fettkenhauer, I. Anusca, M. K. Nazeeruddin, D. C. Lupascu, G. Grancini, *ACS Energy Lett.* **2018**, *3*, 1781.

[50] M. T. Sirtl, F. Ebadi, B. T. van Gorkom, P. Ganswindt, R. A. J. Janssen, T. Bein, W. Tress, *Adv. Opt. Mater.* **2021**, *9*, 23.

[51] P. Chen, Y. Bai, S. Wang, M. Lyu, J. H. Yun, L. Wang, *Adv. Funct. Mater.* **2018**, *28*, 1.

[52] T. Zhang, M. Long, M. Qin, X. Lu, S. Chen, F. Xie, L. Gong, J. Chen, M. Chu, Q. Miao, Z. Chen, W. Xu, P. Liu, W. Xie, J. bin Xu, *Joule* **2018**, *2*, 2706.

[53] Y. Hua, Y. Zhou, D. Hong, S. Wan, X. Hu, D. Xie, Y. Tian, *J. Phys. Chem. Lett.* **2019**, *10*, 7025.

[54] J. A. Sichert, Y. Tong, N. Mutz, M. Vollmer, S. Fischer, K. Z. Milowska, R. García Cortadella, B. Nickel, C. Cardenas-Daw, J. K. Stolarczyk, A. S. Urban, J. Feldmann, *Nano Lett.* **2015**, *15*, 6521.

[55] C. Ortiz-Cervantes, P. Carmona-Monroy, D. Solis-Ibarra, *ChemSusChem* **2019**, *12*, 1560.

[56] P. C. Huang, S. K. Huang, T. C. Lai, M. C. Shih, H. C. Hsu, C. H. Chen, C. C. Lin, C.

H. Chiang, C. Y. Lin, K. Tsukagoshi, C. W. Chen, Y. P. Chiu, S. F. Tsay, Y. C. Wang, *Nano Energy* **2021**, *89*, 106362.

[57] B. A. Connor, L. Leppert, M. D. Smith, J. B. Neaton, H. I. Karunadasa, *J. Am. Chem. Soc.* **2018**, *140*, 5235.

[58] F. Schmitz, J. Horn, N. Dengo, A. E. Sedykh, J. Becker, E. Maiworm, P. Bélteky, Á. Kukovecz, S. Gross, F. Lamberti, K. Müller-Buschbaum, D. Schlettwein, D. Meggiolaro, M. Righetto, T. Gatti, *Chem. Mater.* **2021**, *33*, 4688.

[59] F. Schmitz, R. Neisius, J. Horn, J. Sann, D. Schlettwein, M. Gerhard, T. Gatti, *Nanotechnology* **2022**, *33*, 215706.

[60] R. Hooijer, A. Weis, A. Biewald, M. T. Sirtl, J. Malburg, R. Holfeuer, S. Thamm, A. A. Y. Amin, M. Righetto, A. Hartschuh, L. M. Herz, T. Bein, *Adv. Opt. Mater.* **2022**, *10*, DOI 10.1002/adom.202200354.

[61] W. Sun, J. Zou, X. Wang, S. Wang, Y. Du, F. Cao, L. Zhang, J. Wu, P. Gao, *Nanoscale* **2021**, *13*, 14915.

[62] W. Shi, H. Ye, *J. Phys. Chem. Lett.* **2021**, *12*, 4052.

[63] Q. Zhou, L. Liang, J. Hu, B. Cao, L. Yang, T. Wu, X. Li, B. Zhang, P. Gao, *Adv. Energy Mater.* **2019**, *9*, 1.

[64] X. Wang, Y. Zhao, B. Li, X. Han, Z. Jin, Y. Wang, Q. Zhang, Y. Rui, *ACS Appl. Mater. Interfaces* **2022**, *14*, 22879.

[65] P. Kajal, B. Verma, S. G. R. Vadaga, S. Powar, *Glob. Challenges* **2022**, *6*, DOI 10.1002/gch2.202100070.

[66] N. L. Chang, A. W. Yi Ho-Baillie, P. A. Basore, T. L. Young, R. Evans, R. J. Egan, *Prog. Photovoltaics Res. Appl.* **2017**, *25*, 390.

[67] M. Zhai, C. Chen, M. Cheng, *Sol. Energy* **2023**, *253*, 563.

[68] V. Pecunia, L. G. Occhipinti, R. L. Z. Hoye, *Adv. Energy Mater.* **2021**, *11*, 2100698.

[69] A. Schmitz, L. Leander Schaberg, S. Sirotinskaya, M. Pantaler, D. C. Lupascu, N. Benson, G. Bacher, *ACS Energy Lett.* **2020**, *5*, 559.

[70] M. H. Jung, *J. Mater. Chem. A* **2019**, *7*, 14689.

[71] T. L. Leung, I. Ahmad, A. A. Syed, A. M. C. Ng, J. Popović, A. B. Djurišić, *Commun. Mater.* **2022**, *3*, 1.

[72] E. S. Vasileiadou, B. Wang, I. Spanopoulos, I. Hadar, A. Navrotsky, M. G. Kanatzidis, *J. Am. Chem. Soc.* **2021**, *143*, 2523.

[73] H. Xu, G. Liu, X. Xu, S. Xu, L. Zhang, X. Chen, H. Zheng, X. Pan, *Sol. RRL* **2020**, *4*, 1.

[74] T. M. Koh, V. Shanmugam, X. Guo, S. S. Lim, O. Filonik, E. M. Herzig, P. Müller-Buschbaum, V. Swamy, S. T. Chien, S. G. Mhaisalkar, N. Mathews, *J. Mater. Chem. A* **2018**, *6*, 2122.

[75] C. Li, N. Zhang, P. Gao, *Mater. Chem. Front.* **2023**, DOI 10.1039/D3QM00574G.

[76] Y. Yin, W. Tian, J. Leng, J. Bian, S. Jin, *J. Phys. Chem. Lett.* **2020**, *11*, 6956.

[77] F. Schmitz, N. Lago, L. Fagiolari, J. Burkhart, A. Cester, A. Polo, M. Prato, G. Meneghesso, S. Gross, F. Bella, F. Lamberti, T. Gatti, *Chem. Sustain. Energy Mater.* **2022**, *15*, e202201590.

[78] Y. Yao, B. Kou, Y. Peng, Z. Wu, L. Li, S. Wang, X. Zhang, X. Liu, J. Luo, *Chem. Commun.* **2020**, *56*, 3206.

[79] D. Liu, C. M. Perez, A. S. Vasenko, O. V Prezhdo, *J. Phys. Chem. Lett.* **2022**, *13*, 3645.

[80] Z. He, Q. Tang, X. Liu, X. Yan, K. Li, D. Yue, *Energy and Fuels* **2021**, *35*, 15005.

[81] Z. Xiao, W. Meng, J. Wang, Y. Yan, *Chem. Sustain. Energy Mater.* **2016**, *9*, 2628.

[82] T. Li, X. Zhao, D. Yang, M. Du, L. Zhang, *Phys. Rev. Appl.* **2018**, *10*, DOI 10.1103/PhysRevApplied.10.041001.

[83] Y. She, H. Zhufeng, O. V Prezhdo, W. Li, *J. Phys. Chem. Lett.* **2021**, *12*, 10581.

[84] Z. Zhang, Q. Sun, Y. Lu, F. Lu, X. Mu, S. Wei, M. Sui, *Nat. Commun.* **2022**, *13*, 1.

[85] N. Fairley, V. Fernandez, M. Richard-Plouet, C. Guillot-Deudon, J. Walton, E. Smith, D. Flahaut, M. Greiner, M. Biesinger, S. Tougaard, D. Morgan, J. Baltrusaitis, *Appl. Surf. Sci. Adv.* **2021**, *5*, 100112.

[86] J. P. Perdew, K. Burke, M. Ernzerhof, *Phys. Rev. Lett.* **1996**, *77*, 3865.

[87] G. Kresse, J. Hafner, *Phys. Rev. B* **1993**, *47*, 558.

[88] H. J. Monkhorst, J. D. Pack, *Phys. Rev. B* **1976**, *13*, DOI https://doi.org/10.1103/PhysRevB.13.5188.

Fabian Schmitz, Ribhu Bhatia, Julian Burkhart, Pascal Schweitzer, Marco Allione, Jaime Gallego, Piotr Piotrowski, Jakub Cajzl, Piotr Paszke, Gour Mohan Das, Dorota A. Pawlak, Federico Bella, Derck Schlettwein, Francesco Lamberti, Simone Meloni, Teresa Gatti

Improved hole extraction and band alignment via interface modification in HTM-free Ag/Bi double perovskite solar cells

In this work, we apply a 2D/3D modification through n-butylammonium treatment to a $Cs_2AgBiBr_6$ perovskite thin film to fabricate HTM-free solar cells, bearing carbon black electrodes. The 2D/3D modification improves the band alignment of the perovskite towards the hole selective contact, while strongly reducing the device material- and processing-costs.